PAPER

Check for updates

Rapid separation and purification of lead halide perovskite quantum dots through differential centrifugation in nonpolar solvent†

Shu Zhou [iD] *[ab]

We report the rapid separation and purification of lead halide perovskite quantum dots (QDs) in a nonpolar solvent by using a convenient and efficient differential separation method. Size-selective precipitation effectively separates the perovskite QDs from larger aggregates and provides direct evidence for strong quantum confinement in the photoluminescence (PL). Significantly, the size-selected perovskite QDs are readily well-dispersed in a nonpolar solvent and remain stable in ambient air (humidity > 60%) for >20 days. These enable measurement of the electronic band structure of versatile perovskite QDs as a function of size for the first time. Despite a clear blue-shift of the optical bandgap, the lowest unoccupied molecular orbital (LUMO) readily moves towards the vacuum level while the highest occupied molecular orbital (HOMO) changes slightly, in good agreement with that observed in the quantum size effect tuning of quasi-2D perovskites and colloidal semiconductor QDs. The results demonstrate the possibility of utilizing differential centrifugation as a novel method to attain size-dependent tunability for property-specific perovskite-QD based optoelectronic applications.

Halide perovskites (ABX$_3$, X = Cl, Br, or I) are among the most intensively studied semiconductor materials offering unique electrical and optical properties that are particularly demanded in versatile optoelectronic applications such as lasers, light-emitting diodes (LEDs), photodetectors and solar cells.[1–5] In contrast to conventional semiconductor materials such as Si and Ge,[6,7] the optical properties of halide perovskites can be readily tuned by adjusting their components, *i.e.*, halide content, yielding strong photoluminescence (PL) across the whole visible spectrum.[8] It has been recognized that bright and efficient blue emission plays a key role in the development of halide perovskite LEDs. Current progress in blue perovskite LEDs largely benefits from the component engineering for bandgap tuning, *i.e.*, using mixed halide perovskites.[9,10] Although green and red LEDs incorporating halide perovskites have shown remarkable external quantum efficiency (EQE) over 20%,[11,12] the fabrication of efficient and stable blue LEDs remains challenging largely due to the fact that the blue-emitting perovskites using mixed halide ions usually suffer from severe ion migration and phase segregation under external excitation of light or bias voltage,[13,14] impeding device performance and thereby the niche market application of perovskite

LED technologies. Nevertheless, such a challenge may be confronted by taking advantage of the size-dependent tunability of optical properties in terms of the quantum size effect, *i.e.*, quantum dots (QDs).[15,16] The quantum size effect describes changes in the electronic band structure of a semiconductor as a result of reduction in the dimensionality below a certain threshold.[17–19] The quantum confinement, on one hand, gives rise to a blue-shift of the PL energy. On the other hand, it also causes perovskite QDs to emit light much more efficiently than their bulk counterparts.[20,21]

To meet the requirement of perovskite optoelectronic technologies, effective technical methods to attain size-tunable monodisperse perovskite QDs are still highly desired. To date, many approaches have been developed for synthesizing various kinds of halide perovskite QDs. Kovalenko *et al.* reported a facile hot injection method for colloidal synthesis of CsPbX$_3$ QDs with cubic shape and cubic perovskite crystal structure.[22] Dong *et al.* reported a ligand-assisted re-precipitation colloidal strategy to prepare brightly luminescent and color-tunable CH$_3$NH$_3$PbX$_3$ perovskite QDs with high quantum yields and low excitation fluencies.[23] Petrozza *et al.* demonstrated the synthesis of ligand-free CH$_3$NH$_3$PbX$_3$ perovskite QD inks that are suitable for large-area processing by laser ablation.[24] Ogale *et al.* showed the synthesis of perovskite quantum structures by using an electrospray technique in conjunction with an anti-solvent–solvent extraction.[25] However, many of the synthetic methods produce perovskite QD suspensions with poor morphology and considerable size polydispersity.[26]

*a*School of Materials, Sun Yat-sen University, Guangzhou 510275, China. E-mail: zhoush67@mail.sysu.edu.cn

*b*Department of Physics, The Chinese University of Hong Kong, New Territories, Hong Kong

† Electronic supplementary information (ESI) available. See DOI: 10.1039/d1ra04578d

Consequently, a complex post-synthesis size-purification process is usually required, resulting in significant loss of the perovskite QD products.[27]

Nanoseparation represents an important and effective complementary process to prepare monodisperse nanoparticles for size-dependent electrical and optical properties.[28,29] In particular, differential separation is a centrifugal method based on the different settling velocity of nanoparticles in a homogeneous media that has been widely used especially for the separation and extraction of nanoparticles which contain a big weight difference between the fragments.[30] The separation and purification of metal nanoparticles and typical colloidal semiconductor QDs such as Si and CdSe in organic density gradient have been demonstrated by using differential centrifugation.[29,31,32] However, there have been very few attempts to separate perovskite QDs and the preparation of monodisperse perovskite QDs using size-separation methods is still in its infancy. Thus, knowledge with respect to the definite size-dependent electronic band structure properties of perovskite QDs remains incomplete, in contrast to conventional semiconductor QDs.

In this work, we employ a room-temperature ligand-mediated transport method which is capable of synthesizing a variety of organic-inorganic and inorganic halide perovskite QDs with strong PL (quantum yields (QYs) up to 90%) including $MAPbI_3$, $MAPbBr_3$, $FAPbI_3$, $FAPbBr_3$ and $CsPbBr_3$ QDs (MA = CH_3NH_3, FA = $HC(NH_2)_2$).[33] The obtained perovskite QDs suspended in the crude solutions are surface-terminated by long alkyl chains such as oleic acid and octylamine. We then introduce differential separation as a straightforward and efficient experimental method for preparing monodisperse fractions of perovskite QDs with tunable sizes. Our results reveal that the selection of proper solvents with low polarity is the key for realizing rapid separation and purification of perovskite QDs through differential centrifugation. The size-selected perovskite QDs remained in nonpolar solvents such as hexane and exhibit stable and tunable PL with small band width under ambient air conditions, enabling investigations of their size-dependent electronic band structure properties which is crucial to the development of property-specific perovskite-QD based opto-electronic applications.[34]

Results and discussion

Versatile halide perovskite QDs were synthesized by a room-temperature, ligand-mediated transport method under ambient conditions (Fig. S1 and S2†). Fig. 1a representatively shows the image of a crude solution of $MAPbI_3$ perovskite QDs. Broad optical emission accompanying with multiple peaks expanding from ∼550 to 800 nm is observed in the associated PL spectrum (Fig. 1a). Low magnification transmission electronic microscopy (TEM) image (Fig. 1b) shows spherical particles with considerable size polydispersity, indicating that the crude solution of perovskite QDs contains both big and small particles. High-magnification TEM image (Fig. 1c) demonstrates that the perovskite QDs are consist of a crystalline perovskite core featuring well-defined lattice patterns and consistent with previous report that the perovskite QDs have an orthorhombic crystal structure.[33] Fourier transform infrared (FTIR) spectroscopy measurement demonstrates extensive alkyl termination of the QD surface (Fig. S3†). This high degree of alkyl surface coverage provides perovskite QDs with excellent colloidal stability, an important requirement for size separations. For an ideal spherical nanoparticle with the core density (ρ_c), radius (r), and the shell density (ρ_s), thickness (t) (Fig. 2a), the particle density (ρ_p) may be estimated as[35]

$$\rho_p = \rho_s + (\rho_c - \rho_s)r^3/(r + t)^3 \qquad (1)$$

From the above equation it can be deduced that the ρ_p of a colloidal nanoparticle system would increase when r increases with respect to t. When the nanoparticle is sufficiently large, ρ_p becomes equal to ρ_c. All nanoparticles tend to sediment when they are driven by a centripetal force during spinning. The terminal velocity is determined by r, ρ_p, and the centrifugal force (g) by balancing the centrifugal force against buoyancy and viscous drag. An increase in r, ρ_p, or g would make the
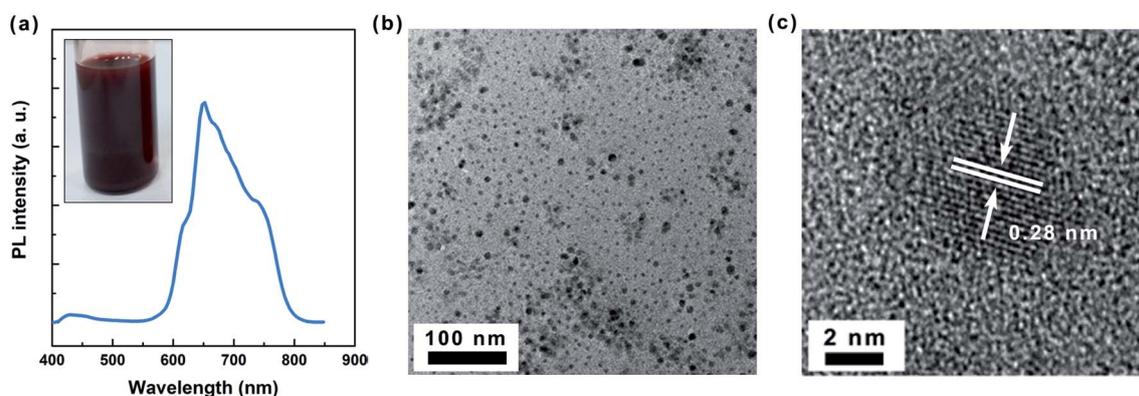

Fig. 1 (a) PL spectrum of the crude solution of $MAPbI_3$ QDs before centrifugation. Inset shows a typical image of the crude solution of $MAPbI_3$ QDs in toluene. (b) Low magnification and (c) high magnification TEM image of $MAPbI_3$ QDs derived from the crude solution showing size polydispersity.
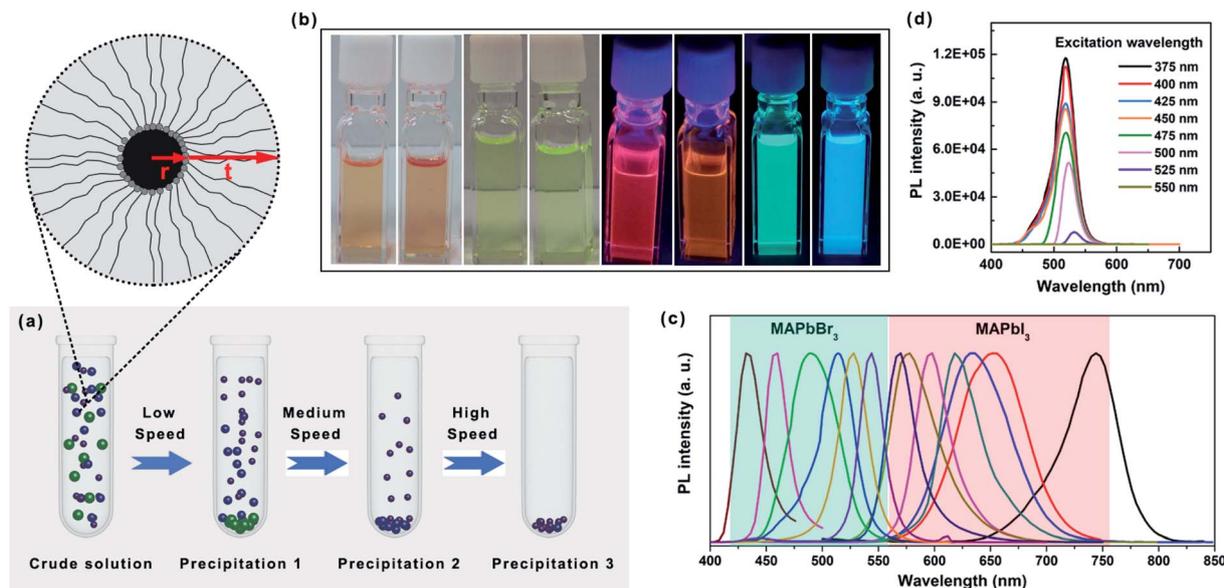
Fig. 2 (a) Schematic illustration of a typical differential size separation method. The structure of a colloidal nanoparticle including an inorganic core and an organic shell is also illustrated. (b) Images of colloidal suspensions of size-selected alkyl-capped MAPbI$_3$ and MAPbBr$_3$ perovskite QDs dispersed in hexane under ambient light (left) and UV light (right). (c) Full-visible PL spectra obtained from the size-selected MAPbI$_3$ and MAPbBr$_3$ perovskite QDs. (d) PL spectra of the MAPbBr$_3$ perovskite QDs dispersed in hexane under different excitaion wavelength.

colloidal nanoparticles sediment faster, and thus promote size separation. Fig. 2a schematically illustrates the differential separation method for rapid separation of perovskite QDs

which is accomplished by repeatedly centrifuging a colloidal suspension from low speed to high speed in order to achieve separation. Specifically, different sized perovskite nanoparticles
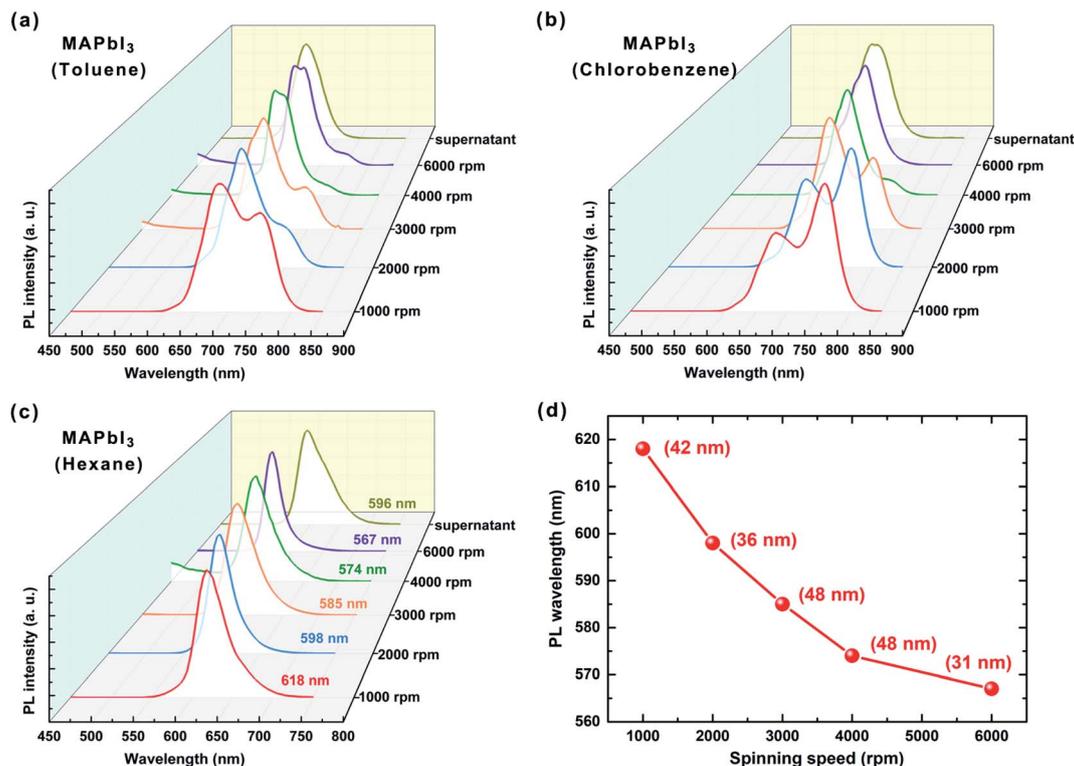

Fig. 3 (a–c) PL spectra of MAPbI$_3$ perovskite QDs obtained from different centrifugation speeds. The solvents for differential separation are toluene (polarity 2.4), chlorobenzene (polarity 2.7) and hexane (polarity 0.06), respectively. (d) The wavelength of the emission peak in (c), summarizing the blue-shift in PL observed with increasing spinning speed. The FWHM for each emission peak is also indicated.

move toward the bottom of centrifuge tube with different settling rates, and the mixture would be gradually separated into two parts, *i.e.*, the large ones in the precipitate and the smaller ones in supernatant. In general, low centrifugation speed was firstly used to precipitate the large perovskite particles to the bottom of the centrifuge tube. After removing the precipitate, higher centrifugation speed was employed for the residual suspension, and small particles would then precipitate.[29]

Fig. 2b representatively shows the PL spectra of size-separated MAPbI$_3$ and MAPbBr$_3$ perovskite QDs obtained from the differential selection. The perovskite QDs exhibit spectrally narrow PL with full-width half maximum (FWHM) of 12–50 nm that is tunable across the full visible spectrum without modifying the component. Fig. 2c shows typical images of colloidal suspensions of the alkyl-capped MAPbI$_3$ and MAPbBr$_3$ perovskite QDs in hexane under ambient light and UV light iradiation. The PL spectra of MAPbBr$_3$ perovskite QDs dispersed in hexane under different excitaion wavelength was shown in Fig. 2d. The QY of the QDs in hexane is measured to be 92%. The strong and bright PL observed in perovskite QDs originates from an increased exciton binding resulting from the quantum confinement given the fact that the excitons that were confined in a small volume could lead to very efficient radiative recombination.[36]

We find that the selection of proper solvent plays a crucial role on the rapid size separation of perovskite QDs through differential separation. Fig. 3 representatively shows the PL

spectra of MAPbI$_3$ QDs extracted from different centrifugation speeds. Particularly, three solvents, *i.e.*, toluene, chlorobenzene and hexane with different polarity were employed for the separation of MAPbI$_3$ QDs by centrifugation. It is found that the use of toluene (polarity 2.4) leads to MAPbI$_3$ QDs with two defined emission peaks (Fig. 3a), suggesting that both large and small QDs precipitate during the spinning process. Subsequently, chlorobenzene (polarity 2.7) was also employed for separation of the same MAPbI$_3$ QDs (Fig. 3b). Similarly, the PL of precipitated MAPbI$_3$ QDs is also featured with two emission peaks. By contrast, the use of hexane (polarity 0.06) leads to PL with a single emission peak. This implies that the polarity of solvent plays the key role for the sequential precipitating of MAPbI$_3$ QDs (Fig. 3c). Impressively, when the spinning speed gradually increases from 1000 rpm to 6000 rpm, the PL peak of MAPbI$_3$ QDs monotonically blue-shifts from 618 nm to 567 nm (Fig. 3d). MAPbI$_3$ QDs with larger size emitting from 618 nm to 750 nm (bulk MAPbI$_3$)[15] cannot be acquired by centrifugation in less than 1000 rpm largely due to the influence of unreacted precursors. In terms of the quantum size effect, the PL wavelength (energy) is directly correlated to the perovskite QD size (*d*) as

$$E_g = E_{bulk} + 3\hbar^2\pi/2m^*d^2 \qquad (2)$$

where E_g is the bandgap of QDs, E_{bulk} is the bandgap of the bulk material, $\hbar$ is the reduced Planck constant, and m^* is the effective mass of carriers.[37] Therefore, a continuous shift of the PL peak toward higher energy implies a monotonic decrease of
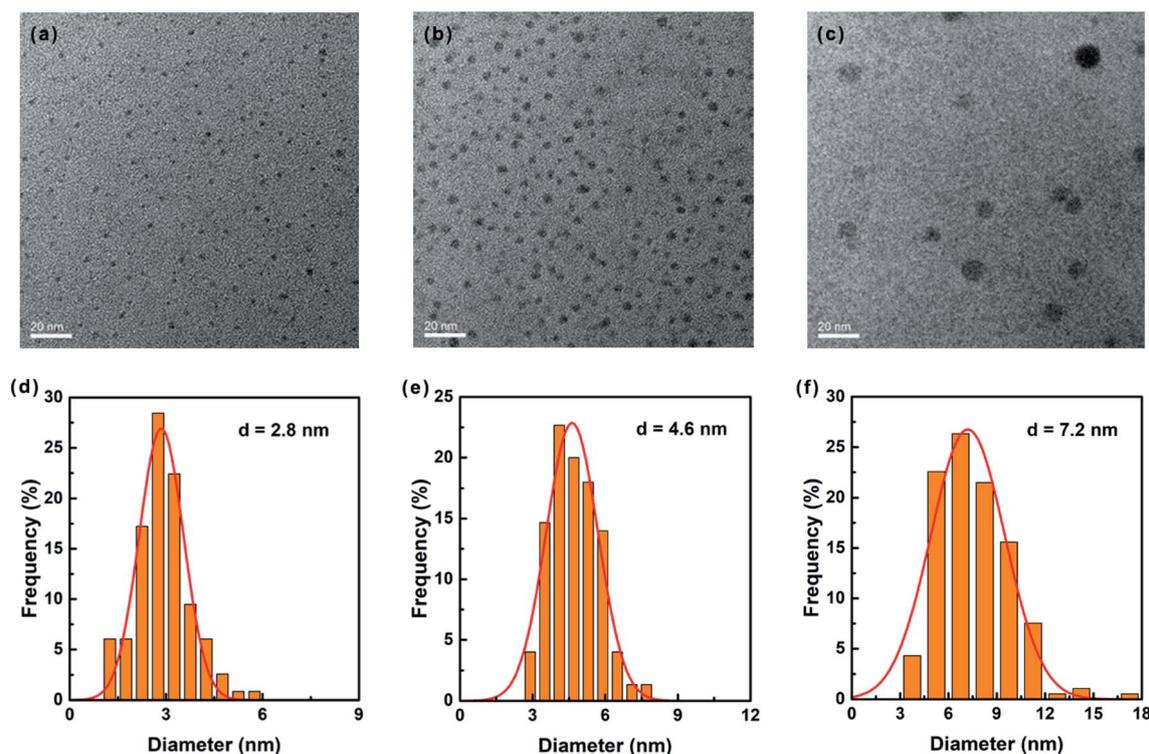

Fig. 4 (a–c) TEM images and (d–f) the corresponding size analysis of monodisperse MAPbI$_3$ perovskite QDs obtained by differential centrifugation.

the QD size, highlighting the effective separation of the MAPbI$_3$ QDs by using centrifugation. The size-selected MAPbI$_3$ QDs exhibit strong PL with small FWHM (<50 nm) which is on par with those reported in the literatures.[22,38] Fig. 4a–c shows the corresponding TEM images of monodisperse MAPbI$_3$ QDs obtained by centrifugation. Size analysis of these perovskite QDs are presented in Fig. 4d–f, respectively. No aggregation of the perovskite QDs is observed, indicating that the organic ligands at the QD surface could give rise to enough steric force to enable well-separated QDs. Similar results have also been observed for the MAPbBr$_3$ QDs, signifying the potential of differential centrifugation on the rapid size selection of perovskite QDs.

It is noteworthy that the size purification through spinning in nonpolar solvent provides better stability for perovskite QDs under ambient air (humidity > 60%), compared with those in polar solvents. Fig. 5a representatively shows the UV-vis absorption spectra of the toluene, chlorobenzene and hexane solutions of MAPbBr$_3$ QDs. Due to the aggregation-induced light scattering, the toluene and chlorobenzene solutions of MAPbBr$_3$ QDs exhibit apparent sub-bandgap optical absorption when the wavelength is >∼540 nm. However, the optical absorbance of hexane solution of MAPbBr$_3$ QDs is almost zero in the long-wavelength region, suggesting their light scattering

is negligible.[39] The stability of MAPbBr$_3$ QDs in toluene, chlorobenzene and hexane can be further investigated by recording the optical absorption of the QD colloids during the course of storage in ambient air (Fig. 5b–d). It can be seen clearly that the optical absorption for toluene and chlorobenzene solutions drops dramatically as the storage time increases to 6 days. By contrast, the optical absorption changes slightly for the hexane solution. Particularly, there is almost no change in absorption spectra of the hexane solution of MAPbBr$_3$ QDs when the storage time further increases up to 20 days. This means that the size-selected perovskite QDs are better dispersed and more stable in hexane than in toluene and chlorobenzene, well consistent with the results present in Fig. 3. Additional UV-Vis study on the MAPbI$_3$ perovskite QDs further confirms their improved stability in nonpolar solvent under ambient condition (Fig. S4†).

Fig. 6 shows the corresponding PL spectra of toluene, chlorobenzene and hexane solutions of MAPbBr$_3$ and MAPbI$_3$ perovskite QDs and the same solutions after stored in air for 6 days and 20 days, respectively. It is found that the PL peaks of all perovskite QD solutions change with the storage time. Notably, the PL peak of MAPbI$_3$ QD hexane solution red-shifts from 652 nm to 668 nm. On the contrary, the PL peak for MAPbBr$_3$
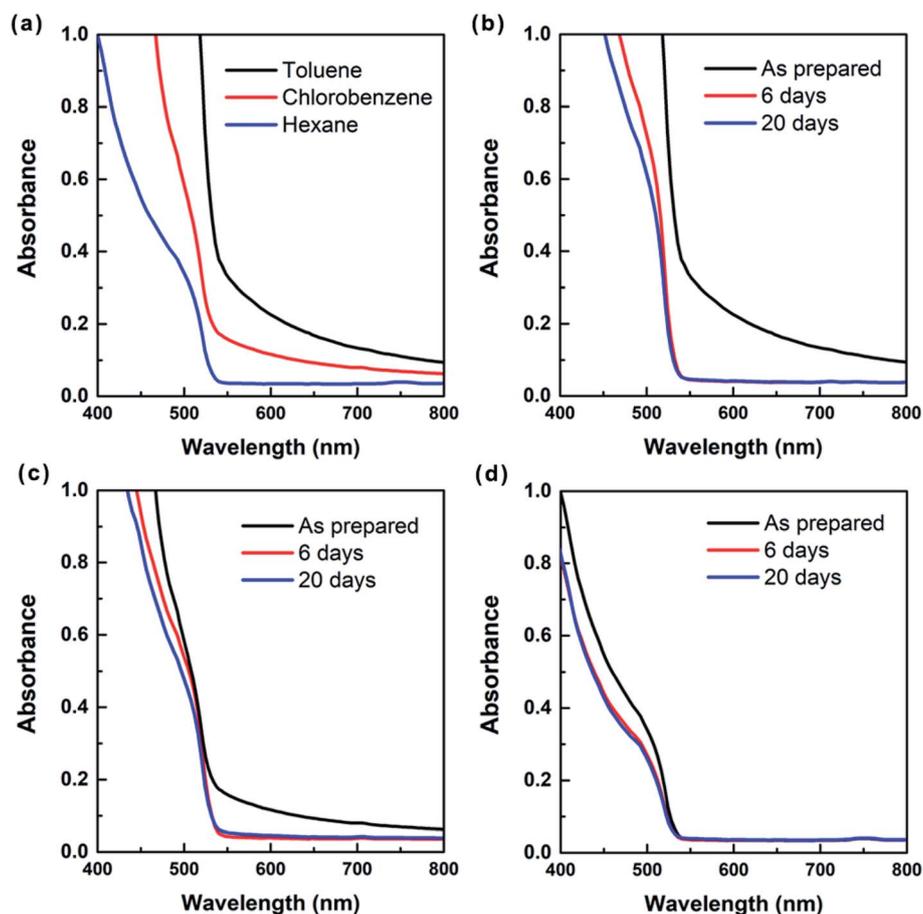

Fig. 5 (a) UV-vis absorption of MAPbBr$_3$ perovskite QDs dispersed in toluene, chlorobenzene and hexane. (b–d) UV-vis absorption of toluene, chlorobenzene and hexane solutions of MAPbBr$_3$ perovskite QDs and the same solutions after stored in air for 6 days and 20 days, respectively.
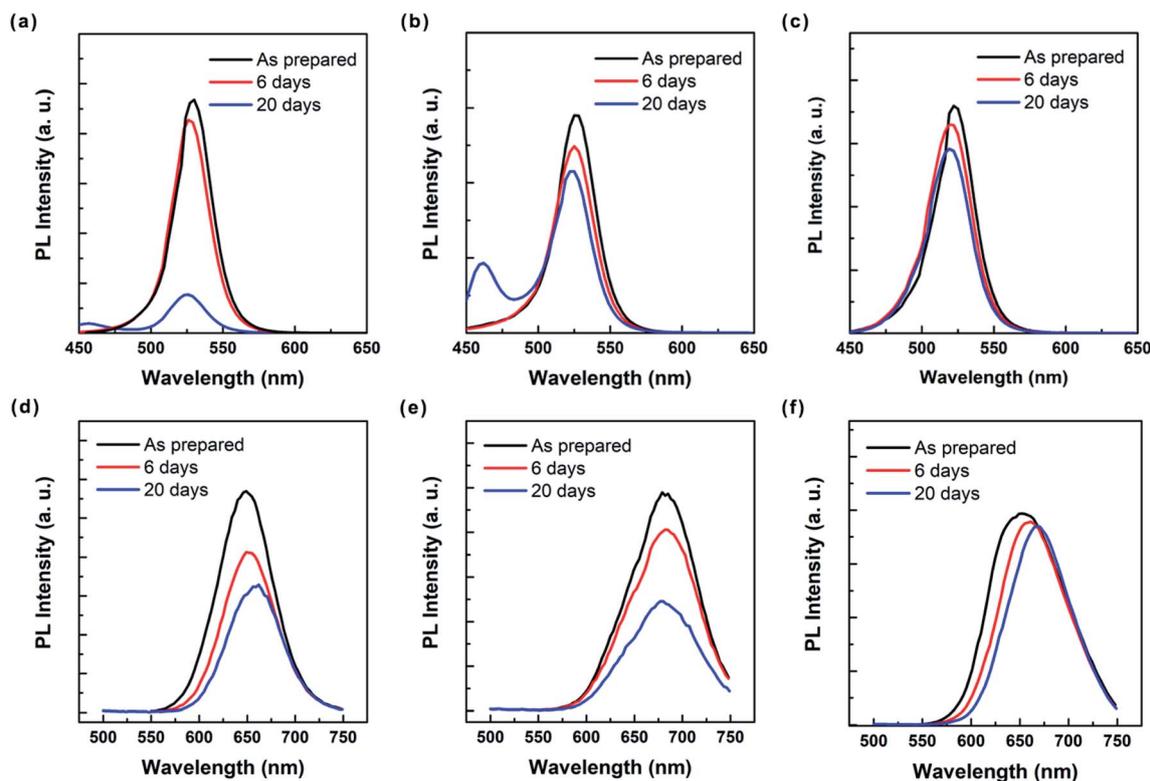
Fig. 6 (a–c) PL spectra of toluene, chlorobenzene and hexane solutions of MAPbBr$_3$ perovskite QDs and the same solutions after stored in ambient air for 6 days and 20 days, respectively. (d–f) PL spectra of toluene, chlorobenzene and hexane solutions of MAPbI$_3$ perovskite QDs and the same solutions after stored in ambient air for 6 days and 20 days, respectively.

QD hexane solution slightly blue-shifts from 522 nm to 519 nm (Fig. S5†). Such a difference suggests the MAPbI$_3$ and MAPbBr$_3$ QDs may experience different transformation processes in the solvents. Considering that trace amount of unreacted precursors may reside in the solutions, the shift of PL peak toward lower energy suggests the MAPbI$_3$ QDs undergo a continuous growth as the time increases, whereas the shift of the PL peak toward higher energy implies that smaller MAPbBr$_3$ QDs tend to nuclear in the solution (Fig. S6†). In addition to the energy shift, the PL intensity drops as the time increases. Specifically, the PL intensity drops by 83%, 25% and 19% after 20 days' storage for the toluene, chlorobenzene and hexane solutions of MAPbBr$_3$ QDs, respectively (Fig. 6a–c). In the meantime, new emission peak centered at ∼460 nm can be found in the PL spectra of toluene and chlorobenzene solutions of MAPbBr$_3$ perovskite QDs, which may be attributed to the formation of small perovskite QDs, as discussed previously. However, no obvious peak at higher energy region appears in the PL spectra of hexane solution of MAPbBr$_3$ QDs. Previous study indicates that excess ligands such as oleic acid degraded the fluorescent perovskite QDs because of promoted crystal growth through dissolution.[40] It appears that the oleic acid residing in the solutions could be more effectively removed by nonpolar solvents than polar solvents, thereby enhancing the stability. For toluene, chlorobenzene and hexane solutions of MAPbI$_3$ QDs we work out that the PL intensity drops by 43%, 50% and 6% after storing for 20 days, respectively (Fig. 6d–f). Intriguingly, no new peaks at higher energy occur to the PL spectra for all solutions of MAPbI$_3$

QDs. Together, it is evident that the perovskite QDs dispersed in hexane are much more stable than those dispersed in toluene and chlorobenzene.

Unlike MAPbI$_3$, MAPbBr$_3$ and CsPbBr$_3$ perovskite QDs (Fig. S7†), it is noted that FAPbBr$_3$ QDs (PL peak at 521 nm) are instable in both non-polar and polar solvents. After stored in air for only 12 hours, the color of the QD solution totally fades out, suggesting the complete dissociation of FAPbBr$_3$ QDs (Fig. S8†). This change is more clearly depicted in the associated absorption and PL spectra (Fig. S8†). It has been previously shown that the crystal structure of MAPbX$_3$ can be maintained even for nanoparticles down to ∼3.3 nm in diameter, but slight structure distortions would occur owing to a dramatic shrinkage of the size and expansion of the specific surface area.[15] For FAPbX$_3$ QDs the structure distortion could be more serious because the size of FA$^+$ is larger than MA$^+$ and Cs$^+$, thereby accelerating the degradation.[41]

Following the stability test, ultraviolet photoelectron spectroscopy (UPS) measurements were performed to study the size-dependent band structures of various perovskite QDs for high-performance optoelectronic devices. Specifically, the highest occupied molecular orbital (HOMO) or Fermi level (E_F) with respect to the vacuum level can be determined by calculating the difference between the excitation energy (130 eV) and the spectrum width or the secondary electron cut-off, respectively (Fig. S9–S11†).[42,43] Combining the optical bandgap (E_{opt}) obtained from the PL spectra (Fig. 7a–c), we are able to illustrate the band structure by using the lowest unoccupied molecular
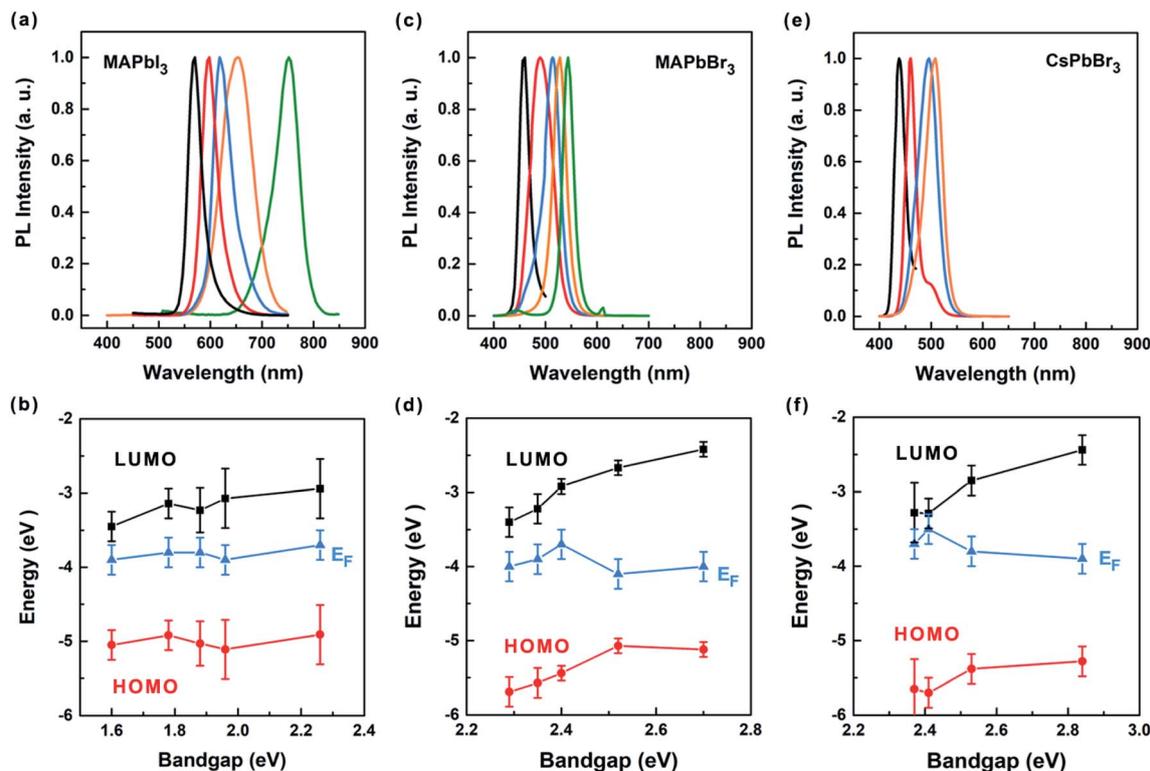
Fig. 7 PL spectra and electronic band structure of the size-selected monodisperse (a and b) MAPbI$_3$, (c and d) MAPbBr$_3$ and (e and f) CsPbBr$_3$ perovskite QDs. The HOMO, LUMO, and E_F energies are measured from the vacuum level of the perovskite QDs by using UPS combined with PL spectroscopy.

orbital (LUMO) deduced from the HOMO and the optical bandgaps (LUMO = HOMO + E_{opt}). Fig. 7d–f shows the energies for the HOMO, LUMO and E_F of the size-selected MAPbI$_3$, MAPbBr$_3$ and CsPbBr$_3$ perovskite QDs, respectively. For all perovskite QDs, it is observed that the QD size reduction (increase of bandgap) leads to significant shift of the LUMO towards the vacuum level. Compared with the LUMO, the HOMO changes less obvious with the QD size. This implies that the quantum confinement more seriously impacts the LUMO than the HOMO for the perovskite QDs. This phenomenon is quite similar to what has been observed in the quantum size effect tuning of quasi-2D perovskites and colloidal quantum dots.[44,45] For MAPbI$_3$ perovskite QDs, the E_F lies closer to the LUMO than HOMO, showing n-type behavior that is independent of the size. The n-type behavior is likely induced by defects or organic ligands existed at the QD surface, as indicated in previous works.[46,47] Compared with MAPbI$_3$ perovskite QDs, the E_F moves towards the HOMO more seriously for MAPbBr$_3$ and CsPbBr$_3$ QDs as the size decreases, manifesting an electronic transition from n-type to intrinsic behavior. It appears that the n-type behavior could be mitigated for smaller perovskite QDs owing to a larger shift of the LUMO than HOMO caused by the quantum size effect.

Conclusions

In conclusion, we report the rapid separation and purification of lead halide perovskite QDs by using a simple differential centrifugation method different from what has been reported for conventional semiconductor QDs in which complex organic density gradients are required. Such efficient selection of QD size is found to be enabled by the choice of proper solvent with low polarity. In particular, the option of nonpolar solvent such as hexane yields monodispersed perovskite QDs with tunable size and narrow size distributions, whereas the use of polar solvents such as toluene and chlorobenzene leads to perovskite QDs with broad size distributions and PL with multiple peaks. Importantly, the size-selected perovskite QDs are readily well-dispersed in nonpolar solvent which remains stable in humidity air for more than 20 days. These monodisperse and stable perovskite QDs provide a good platform for study of their size-dependent band structure properties. It is revealed that the quantum confinement more significantly impacts the LUMO than the HOMO for the perovskite QDs which results in the evolution from an n-type behavior for big QDs to an intrinsic behavior for small QDs. We expect that the current experimental progress should contribute to the development of versatile property-specific perovskite-QD based optoelectronic applications.

Experimental methods

Materials

Methylammonium bromide (MABr, 99.9%, Dyesol), methylammonium iodide (MAI, 99.9%, Dyesol), formamidinium bromide (FABr, 99.9%, Dyesol), formamidinium iodide (FAI,

99.9%, Dyesol), cesium bromide (CsBr, Sigma-Aldrich, 99%, metals basis), lead(II) bromide ($PbBr_2$, Sigma-Aldrich, 99%, metals basis), lead(II) iodide (PbI_2, Sigma-Aldrich, 99%, metals basis), octylamine (Aladdin, 99.5%), oleic acid (Aladdin, 99.5%), hexane (Sigma-Aldrich, 95%), toluene (Sigma-Aldrich, anhydrous, 99.8%), chlorobenzene (Sigma-Aldrich, 99.9%).

Synthesis of halide perovskite QDs

For synthesis of $MAPbI_3$ QDs, 6.3 mg (0.04 mmol) CH_3NH_3I and 23.0 mg (0.05 mmol) PbI_2 were added into a 10 mL scintillation vial. Subsequently, 2 mL toluene/chlorobenzene/hexane, 10 μL octylamine, and 20 μL oleic acid were added to the solid precursors. The resulting mixture was stirred vigorously under ambient conditions for 2 h, followed by standing for 10 min to remove the residing solid precursors. A crude solution of $MAPbI_3$ QDs was obtained.

For synthesis of $MAPbBr_3$, $FAPbI_3$ and $CsPbBr_3$ QDs, 4.5 mg (0.04 mmol) CH_3NH_3Br and 18.7 mg (0.05 mmol) $PbBr_2$, 7.0 mg (0.04 mmol) $CH(NH_2)_2I$ and 23.0 mg (0.05 mmol) PbI_2, and 8.5 mg (0.04 mmol) CsBr and 18.7 mg (0.05 mmol) $PbBr_2$ were employed as solid precursors, respectively. 2 mL toluene/chlorobenzene/hexane, 10 μL octylamine, and 20 μL oleic acid were then added to the solid precursors. The resulting mixtures were stirred vigorously under ambient conditions for 2 h, followed by standing for 10 min to remove the residing solid precursors. A crude solution of $MAPbBr_3$/$FAPbI_3$/$CsPbBr_3$ QDs was obtained.

Differential ultracentrifugation separation

The crude solution of perovskite QDs was firstly transferred to a centrifuge tube after storing for 1 h and was centrifugated at a low speed (500 rpm) to remove unreacted precursors. A centrifugation speed of 1000 rpm was then used to precipitate the large QDs to the bottom of the tube. The large QDs were collected and re-dispersed in solvent for further characterizations. Subsequently, higher centrifugation speed (2000–6000 rpm) was used for the residual suspension, and small QDs would precipitate to the bottom of the tube. The small QDs were then collected and re-dispersed in solvent for further characterizations.

Characterizations

TEM images were recorded by FEI Tecnai Spirit microscope operated at an acceleration voltage of 200 kV. Steady state PL measurements were performed by using SpectraMax M5e. A UV-vis spectrometer (Hitachi U-3501) was used to measure the optical absorption of all perovskite QD solutions. UPS measurements were performed at BL09A2 U5 beamline at the National Synchrotron Radiation Research Center, Taiwan. UPS measurements were carried out with an excitation energy of 130 eV and a −4 eV bias. Samples for UPS were prepared by placing the perovskite QDs on a 8 mm × 8 mm ITO substrate. FTIR measurements were performed by using a spectrometer (JASCO FT/IR-6100) operated in the transmission mode with a resolution of 4 cm^{-1}. Samples for FTIR measurements were prepared by drop-casting the perovskite QD colloid on a KBr substrate.

Author contributions

S. Zhou conceived the idea. S. Zhou conducted the experiments and coordinated the experiments. All authors discussed and commented on the paper.

Conflicts of interest

There are no conflicts to declare.

Acknowledgements

References

1 M. V. Kovalenko, L. Protesescu and M. I. Bodnarchuk, Properties and potential optoelectronic applications of lead halide perovskite nanocrystals, *Science*, 2017, **358**, 745–750.

2 Q. A. Akkerman, G. Rainò, M. V. Kovalenko and L. Manna, Genesis, challenges and opportunities for colloidal lead halide perovskite nanocrystals, *Nat. Mater.*, 2018, **17**, 394–405.

3 H. Huang, M. I. Bodnarchuk, S. V. Kershaw, M. V. Kovalenko and A. L. Rogach, Lead Halide Perovskite Nanocrystals in the Research Spotlight: Stability and Defect Tolerance, *ACS Energy Lett.*, 2017, **2**, 2071–2083.

4 J. Li, L. Xu, T. Wang, J. Song, J. Chen, J. Xue, Y. Dong, B. Cai, Q. Shan, B. Han and H. Zeng, 50-Fold EQE Improvement up to 6.27% of Solution-Processed All-Inorganic Perovskite $CsPbBr_3$ QLEDs *via* Surface Ligand Density Control, *Adv. Mater.*, 2017, **29**, 1603885.

5 Q. Chen, J. Wu, X. Ou, B. Huang, J. Almutlaq, A. A. Zhumekenov, X. Guan, S. Han, L. Liang, Z. Yi, J. Li, X. Xie, Y. Wang, Y. Li, D. Fan, D. B. L. Teh, A. H. All, O. F. Mohammed, O. M. Bakr, T. Wu, M. Bettinelli, H. Yang, W. Huang and X. Liu, All-inorganic perovskite nanocrystal scintillators, *Nature*, 2018, **561**, 88–93.

6 Z. Y. Ni, S. Zhou, S. Y. Zhao, W. B. Peng, D. R. Yang and X. D. Pi, Silicon nanocrystals: unfading silicon materials for optoelectronics, *Mater. Sci. Eng., R*, 2019, **138**, 85–117.

7 D. Carolan, Recent advances in germanium nanocrystals: synthesis, optical properties and applications, *Prog. Mater. Sci.*, 2017, **90**, 128–158.

8 B. R. Sutherland and E. H. Sargent, Perovskite photonic sources, *Nat. Photonics*, 2016, **10**, 295–302.

9 M. Karlsson, Z. Yi, S. Reichert, X. Luo, W. Lin, Z. Zhang, C. Bao, R. Zhang, S. Bai, G. Zheng, P. Teng, L. Duan, Y. Lu, K. Zheng, T. Pullerits, C. Deibel, W. Xu, R. Friend and

F. Gao, Mixed halide perovskites for spectrally stable and high-efficiency blue light-emitting diodes, *Nat. Commun.*, 2021, **12**, 361.

10 X. Zheng, S. Yuan, J. Liu, J. Yin, F. Yuan, W.-S. Shen, K. Yao, M. Wei, C. Zhou, K. Song, B.-B. Zhang, Y. Lin, M. N. Hedhili, N. Wehbe, Y. Han, H.-T. Sun, Z.-H. Lu, T. D. Anthopoulos, O. F. Mohammed, E. H. Sargent, L.-S. Liao and O. M. Bakr, Chlorine Vacancy Passivation in Mixed Halide Perovskite Quantum Dots by Organic Pseudohalides Enables Efficient Rec. 2020 Blue Light-Emitting Diodes, *ACS Energy Lett.*, 2020, **5**, 793–798.

11 K. Lin, J. Xing, L. N. Quan, F. P. G. de Arquer, X. Gong, J. Lu, L. Xie, W. Zhao, D. Zhang, C. Yan, W. Li, X. Liu, Y. Lu, J. Kirman, E. H. Sargent, Q. Xiong and Z. Wei, Perovskite light-emitting diodes with external quantum efficiency exceeding 20 percent, *Nature*, 2018, **562**, 245–248.

12 Y. Cao, N. Wang, H. Tian, J. Guo, Y. Wei, H. Chen, Y. Miao, W. Zou, K. Pan, Y. He, H. Cao, Y. Ke, M. Xu, Y. Wang, M. Yang, K. Du, Z. Fu, D. Kong, D. Dai, Y. Jin, G. Li, H. Li, Q. Peng, J. Wang and W. Huang, Perovskite light-emitting diodes based on spontaneously formed submicrometre-scale structures, *Nature*, 2018, **562**, 249–253.

13 H. Zhang, X. Fu, Y. Tang, H. Wang, C. Zhang, W. W. Yu, X. Wang, Y. Zhang and M. Xiao, Phase segregation due to ion migration in all-inorganic mixed-halide perovskite nanocrystals, *Nat. Commun.*, 2019, **10**, 1088.

14 P. Vashishtha and J. E. Halpert, Field-Driven Ion Migration and Color Instability in Red-Emitting Mixed Halide Perovskite Nanocrystal Light-Emitting Diodes, *Chem. Mater.*, 2017, **29**, 5965–5973.

15 V. Malgras, S. Tominaka, J. W. Ryan, J. Henzie, T. Takei, K. Ohara and Y. Yamauchi, Observation of Quantum Confinement in Monodisperse Methylammonium Lead Halide Perovskite Nanocrystals Embedded in Mesoporous Silica, *J. Am. Chem. Soc.*, 2016, **138**, 13874–13881.

16 Y. Liu, J. Cui, K. Du, H. Tian, Z. He, Q. Zhou, Z. Yang, Y. Deng, D. Chen, X. Zuo, Y. Ren, L. Wang, H. Zhu, B. Zhao, D. Di, J. Wang, R. H. Friend and Y. Jin, Efficient blue light-emitting diodes based on quantum-confined bromide perovskite nanostructures, *Nat. Photonics*, 2019, **13**, 760–764.

17 S. Repp, S. Weber and E. Erdem, Defect Evolution of Nonstoichiometric ZnO Quantum Dots, *J. Phys. Chem. C*, 2016, **120**, 25124–25130.

18 P. Jakes and E. Erdem, Finite size effects in ZnO nanoparticles: An electron paramagnetic resonance (EPR) analysis, *Phys. Status Solidi RRL*, 2011, **5**, 56–58.

19 S. Repp and E. Erdem, Controlling the exciton energy of zinc oxide (ZnO) quantum dots by changing the confinement conditions, *Spectrochim. Acta, Part A*, 2016, **152**, 637–644.

20 N. Mondal, A. De and A. Samanta, Achieving Near-Unity Photoluminescence Efficiency for Blue-Violet-Emitting Perovskite Nanocrystals, *ACS Energy Lett.*, 2019, **4**, 32–39.

21 J. Pan, Y. Shang, J. Yin, M. De Bastiani, W. Peng, I. Dursun, L. Sinatra, A. M. El-Zohry, M. N. Hedhili, A.-H. Emwas, O. F. Mohammed, Z. Ning and O. M. Bakr, Bidentate Ligand-Passivated CsPbI$_3$ Perovskite Nanocrystals for Stable Near-Unity Photoluminescence Quantum Yield and Efficient Red Light-Emitting Diodes, *J. Am. Chem. Soc.*, 2018, **140**, 562–565.

22 L. Protesescu, S. Yakunin, M. I. Bodnarchuk, F. Krieg, R. Caputo, C. H. Hendon, R. X. Yang, A. Walsh and M. V. Kovalenko, Nanocrystals of Cesium Lead Halide Perovskites (CsPbX$_3$, X = Cl, Br, and I): Novel Optoelectronic Materials Showing Bright Emission with Wide Color Gamut, *Nano Lett.*, 2015, **15**, 3692–3696.

23 F. Zhang, H. Zhong, C. Chen, X.-g. Wu, X. Hu, H. Huang, J. Han, B. Zou and Y. Dong, Brightly Luminescent and Color-Tunable Colloidal CH$_3$NH$_3$PbX$_3$ (X = Br, I, Cl) Quantum Dots: Potential Alternatives for Display Technology, *ACS Nano*, 2015, **9**, 4533–4542.

24 F. Lamberti, L. Litti, M. De Bastiani, R. Sorrentino, M. Gandini, M. Meneghetti and A. Petrozza, High-Quality, Ligands-Free, Mixed-Halide Perovskite Nanocrystals Inks for Optoelectronic Applications, *Adv. Energy Mater.*, 2017, **7**, 1601703.

25 R. Naphade, S. Nagane, G. S. Shanker, R. Fernandes, D. Kothari, Y. Zhou, N. P. Padture and S. Ogale, Hybrid Perovskite Quantum Nanostructures Synthesized by Electrospray Antisolvent–Solvent Extraction and Intercalation, *ACS Appl. Mater. Interfaces*, 2016, **8**, 854–861.

26 C. K. Ng, C. Wang and J. J. Jasieniak, Synthetic Evolution of Colloidal Metal Halide Perovskite Nanocrystals, *Langmuir*, 2019, **35**, 11609–11628.

27 J. Shamsi, A. S. Urban, M. Imran, L. De Trizio and L. Manna, Metal Halide Perovskite Nanocrystals: Synthesis, Post-Synthesis Modifications, and Their Optical Properties, *Chem. Rev.*, 2019, **119**, 3296–3348.

28 G. Chen, Y. Wang, L. H. Tan, M. Yang, L. S. Tan, Y. Chen and H. Chen, High-Purity Separation of Gold Nanoparticle Dimers and Trimers, *J. Am. Chem. Soc.*, 2009, **131**, 4218–4219.

29 P. Li, A. Kumar, J. Ma, Y. Kuang, L. Luo and X. Sun, Density gradient ultracentrifugation for colloidal nanostructures separation and investigation, *Sci. Bull.*, 2018, **63**, 645–662.

30 J. A. Jamison, K. M. Krueger, C. T. Yavuz, J. T. Mayo, D. LeCrone, J. J. Redden and V. L. Colvin, Size-Dependent Sedimentation Properties of Nanocrystals, *ACS Nano*, 2008, **2**, 311–319.

31 M. L. Mastronardi, F. Hennrich, E. J. Henderson, F. Maier-Flaig, C. Blum, J. Reichenbach, U. Lemmer, C. Kübel, D. Wang, M. M. Kappes and G. A. Ozin, Preparation of Monodisperse Silicon Nanocrystals Using Density Gradient Ultracentrifugation, *J. Am. Chem. Soc.*, 2011, **133**, 11928–11931.

32 L. Bai, X. Ma, J. Liu, X. Sun, D. Zhao and D. G. Evans, Rapid Separation and Purification of Nanoparticles in Organic Density Gradients, *J. Am. Chem. Soc.*, 2010, **132**, 2333–2337.

33 L. Wang, N. E. Williams, E. W. Malachosky, J. P. Otto, D. Hayes, R. E. Wood, P. Guyot-Sionnest and G. S. Engel, Scalable Ligand-Mediated Transport Synthesis of Organic–Inorganic Hybrid Perovskite Nanocrystals with Resolved Electronic Structure and Ultrafast Dynamics, *ACS Nano*, 2017, **11**, 2689–2696.

34 G. Rainò, M. A. Becker, M. I. Bodnarchuk, R. F. Mahrt, M. V. Kovalenko and T. Stöferle, Superfluorescence from lead halide perovskite quantum dot superlattices, *Nature*, 2018, **563**, 671–675.

35 X. Sun, S. M. Tabakman, W.-S. Seo, L. Zhang, G. Zhang, S. Sherlock, L. Bai and H. Dai, Separation of Nanoparticles in a Density Gradient: FeCo@C and Gold Nanocrystals, *Angew. Chem., Int. Ed.*, 2009, **48**, 939–942.

36 Y. Li, X. Luo, T. Ding, X. Lu and K. Wu, Size- and Halide-Dependent Auger Recombination in Lead Halide Perovskite Nanocrystals, *Angew. Chem., Int. Ed.*, 2020, **59**, 14292–14295.

37 D. Di, K. P. Musselman, G. Li, A. Sadhanala, Y. Ievskaya, Q. Song, Z.-K. Tan, M. L. Lai, J. L. MacManus-Driscoll, N. C. Greenham and R. H. Friend, Size-Dependent Photon Emission from Organometal Halide Perovskite Nanocrystals Embedded in an Organic Matrix, *J. Phys. Chem. Lett.*, 2015, **6**, 446–450.

38 E. M. Sanehira, A. R. Marshall, J. A. Christians, S. P. Harvey, P. N. Ciesielski, L. M. Wheeler, P. Schulz, L. Y. Lin, M. C. Beard and J. M. Luther, Enhanced mobility CsPbI$_3$ quantum dot arrays for record-efficiency, high-voltage photovoltaic cells, *Sci. Adv.*, 2017, **3**, eaao4204.

39 S. Zhou, Z. Ni, Y. Ding, M. Sugaya, X. Pi and T. Nozaki, Ligand-Free, Colloidal, and Plasmonic Silicon Nanocrystals Heavily Doped with Boron, *ACS Photonics*, 2016, **3**, 415–422.

40 T. Kosugi, Y. Iso and T. Isobe, Effects of Oleic Acid on the Stability of Perovskite CsPbBr$_3$ Quantum Dot Dispersions, *Chem. Lett.*, 2019, **48**, 349–352.

41 Q. A. Akkerman and L. Manna, What Defines a Halide Perovskite?, *ACS Energy Lett.*, 2020, **5**, 604–610.

42 S. Zhou, Y. Ma, G. Zhou, X. Xu, M. Qin, Y. Li, Y.-J. Hsu, H. Hu, G. Li, N. Zhao, J. Xu and X. Lu, Ag-Doped Halide Perovskite Nanocrystals for Tunable Band Structure and Efficient Charge Transport, *ACS Energy Lett.*, 2019, **4**, 534–541.

43 S. Zhou, G. Zhou, Y. Li, X. Xu, Y.-J. Hsu, J. Xu, N. Zhao and X. Lu, Understanding Charge Transport in All-Inorganic Halide Perovskite Nanocrystal Thin-Film Field Effect Transistors, *ACS Energy Lett.*, 2020, **5**, 2614–2623.

44 M. Yuan, L. N. Quan, R. Comin, G. Walters, R. Sabatini, O. Voznyy, S. Hoogland, Y. Zhao, E. M. Beauregard, P. Kanjanaboos, Z. Lu, D. H. Kim and E. H. Sargent, Perovskite energy funnels for efficient light-emitting diodes, *Nat. Nanotechnol.*, 2016, **11**, 872–877.

45 J. Jasieniak, M. Califano and S. E. Watkins, Size-Dependent Valence and Conduction Band-Edge Energies of Semiconductor Nanocrystals, *ACS Nano*, 2011, **5**, 5888–5902.

46 T. Shi, W.-J. Yin, F. Hong, K. Zhu and Y. Yan, Unipolar self-doping behavior in perovskite CH$_3$NH$_3$PbBr$_3$, *Appl. Phys. Lett.*, 2015, **106**, 103902.

47 E. A. Gaulding, J. Hao, H. S. Kang, E. M. Miller, S. N. Habisreutinger, Q. Zhao, A. Hazarika, P. C. Sercel, J. M. Luther and J. L. Blackburn, Conductivity Tuning *via* Doping with Electron Donating and Withdrawing Molecules in Perovskite CsPbI$_3$ Nanocrystal Films, *Adv. Mater.*, 2019, **31**, 1902250.